Geophysical Journal International

Geophys. J. Int. (2016) **204,** 1222–1236 doi: 10.1093/gji/ggv516
GJI Seismology

Global tomography using seismic hum

A. Haned,[1,2] E. Stutzmann,[1] M. Schimmel,[3] S. Kiselev,[4] A. Davaille[5] and A. Yelles-Chaouche[2]

[1] *Institut de Physique du Globe de Paris, PRES Sorbonne Paris Cité, 1 rue Jussieu, F-75005 Paris, France. E-mail: stutz@ipgp.fr*
[2] *Centre de Recherche en Astronomie Astrophysique et Geophysique, Route de l'Observatoire, BP 63, Bouzareah, Algiers, Algeria*
[3] *Institute of Earth Sciences Jaume Almera, CSIC, Lluis Sole i Sabaris s/n, E-08028 Barcelona, Spain*
[4] *Institute of Physics of the Earth, Bolshaya Gruzinskaya str., 10-1 Moscow 123242, Russia*
[5] *Laboratoire FAST, Univ. Paris-Sud/CNRS, Bat 502, rue du Belvedere, Campus Universitaire, F-91405, Orsay, France*

Accepted 2015 November 26. Received 2015 November 12; in original form 2015 April 24

SUMMARY

We present a new upper-mantle tomographic model derived solely from hum seismic data. Phase correlograms between station pairs are computed to extract phase-coherent signals. Correlograms are then stacked using the time–frequency phase-weighted stack method to build-up empirical Green's functions. Group velocities and uncertainties are measured in the wide period band of 30–250 s, following a resampling approach. Less data are required to extract reliable group velocities at short periods than at long periods, and 2 yr of data are necessary to measure reliable group velocities for the entire period band. Group velocities are first regionalized and then inverted *versus* depth using a simulated annealing method in which the number and shape of splines that describes the *S*-wave velocity model are variable. The new *S*-wave velocity tomographic model is well correlated with models derived from earthquakes in most areas, although in India, the Dharwar craton is shallower than in other published models.

Key words: Time-series analysis; Surface waves and free oscillations; Seismic tomography.

1 INTRODUCTION

Over the last 30 yr, progress in imaging the Earth has been driven by the growing amounts of earthquake data and by theoretical and numerical improvements to tomographic techniques. There is increasing agreement between tomographic models on the large-scale elastic structure of the Earth, but the intermodel correlations remain low for the small-scale structure (see Moulik & Ekström 2014, for a review). One limitation is the non-uniform Earth coverage that results from earthquake distributions remaining mainly along plate boundaries.

It has been shown theoretically that empirical Green's functions (EGFs) can be extracted from seismic noise cross-correlations between stations pairs (Lobkis & Weaver 2001; Derode *et al.* 2003; Snieder 2004; Wapenaar 2004). The use of noise correlations provides a good alternative or a complementary data set for improvements to the resolution of tomographic models, because the corresponding path coverage only depends on the station locations. Shapiro *et al.* (2005) and Sabra *et al.* (2005) first demonstrated that this technique can be applied to regional tomography. Since these pioneer studies, noise mostly in the period band of 3–100 s has been extensively used for local and regional tomographic studies and also to complement earthquake data sets (e.g. Bensen *et al.* 2008; Dias *et al.* 2015). Nishida *et al.* (2009) further showed that longer period noise (i.e. 150–250 s) can be used for global tomography.

Noise in the period band of 1–250 s can be separated into so-called primary and secondary microseisms and hum. The source mechanisms of primary and secondary microseisms are well understood (Longuet-Higgins 1950; Hasselmann 1963). Primary microseisms (i.e. with periods of 10–20 s) are generated by interactions between ocean gravity waves with bathymetry at the coast, whereas secondary microseisms (i.e. with periods of 3–12 s) are generated by the mutual interactions of ocean gravity waves. Secondary microseisms have been successfully modelled considering pressure sources close to the ocean surface (e.g. Kedar *et al.* 2008; Ardhuin *et al.* 2011; Stutzmann *et al.* 2012). Longer period noise (i.e. 30–250 s), which is known as hum, is several orders of magnitude weaker than microseisms. The hum source mechanism remains controversial (Rhie & Romanowicz 2004; Tanimoto 2005; Webb 2007; Nishida 2013; Traer & Gerstoft 2014), although recently Ardhuin *et al.* (2015) showed that it can be modelled between 30 and 250 s, considering pressure sources generated by the interactions of infragravity waves with continental shelves.

Ideally, cross-correlation can only retrieve the EGFs for systems with equipartitioned waves (Weaver & Lobkis 2006). As noise sources are mostly located in the oceans and are not randomly distributed, the equipartition of waves is not guaranteed. Therefore, averaging cross-correlograms over long-time spans is necessary to improve the emergence of the EGF (e.g. Shapiro *et al.* 2005). Schimmel *et al.* (2011) proposed a new approach that was based on the instantaneous phase of the analytical signal to improve EGF

recovery and to increase its signal-to-noise ratio. They successfully applied this to selected stations from the global GEOSCOPE network, and they were able to extract the first and second Rayleigh wave trains from the noise in the period band of 25–330 s.

The purpose of this study is to derive a new global tomographic model of the upper mantle using only hum data. We use the method of Schimmel *et al.* (2011) to extract EGF in the wide period band of 30–250 s at the global scale. We use a statistical approach to measure the group velocities (Schimmel *et al.* 2015). The global maps of group velocities are then inverted to obtain the three-dimensional (3-D) *S*-wave velocity model using a simulated annealing method in which the number and shape of splines that describe the model vary within the inversion (e.g. Sambridge *et al.* 2013). This model is derived solely from seismic hum in the wide period band of 30–250 s, and it can be used to study the upper-mantle structure as independent and complementary observations, with respect to models derived from earthquake measurements.

2 METHOD

2.1 Empirical Green's function estimation

For a pair of stations, the EGF is extracted from the seismic-noise cross-correlograms. The data processing steps are: (1) pre-processing, (2) cross-correlation and (3) cross-correlogram stacking. Classical methods (e.g. the classical correlation and stack [CCS] method; Bensen *et al.* (2007)) usually require pre-processing, such as 1-bit normalisation and spectral whitening of the data, to remove the influence of large-amplitude signals such as earthquakes. Correlograms are then computed between seismograms recorded by station pairs and linearly stacked.

Here, we use different data processing to obtain the EGFs. This is based on analytical signal theory and we compute the phase correlation followed by the phase weighted stack, as proposed by Schimmel *et al.* (2011). This method is called hereafter the PCPWS (i.e. phase correlation, phase weighted stack) method and does not require pre-processing for down-weighting earthquakes, because the phase correlation is amplitude unbiased.

For each station, continuous vertical seismograms sampled at 1 Hz are selected and cut into 24-hr segments. Instrumental responses are removed and the data are converted into velocities. No further pre-processing is applied to the data.

For each station pair, phase correlograms between daily seismograms are computed as follows. Considering the seismogram $u(t)$ as a function of time t, the analytical signal is given by $s(t) = u(t) + iH(u(t)) = A(t)\exp(i\phi(t))$, where $H(u(t))$ is the Hilbert transform of $u(t)$. $A(t)$ and $\phi(t)$ are the instantaneous envelope and phase, respectively. Considering two time-series $u(t)$ and $v(t)$, starting at time τ_0 and with duration T, and their instantaneous phases $\Phi(t)$ and $\Psi(t)$, the phase cross-correlation is defined as (Schimmel 1999):

$$C_{\mathrm{PCC}}(\tau) = \frac{1}{2T}\sum_{t=\tau+\tau_0}^{T-\tau+\tau_0}\left(|e^{i\Phi(t+\tau)} + e^{i\Psi(t)}|^{\nu} - |e^{i\Phi(t+\tau)} - e^{i\Psi(t)}|^{\nu}\right) \quad (1)$$

where τ is the time lag, t is the time, T is the length of the correlation window, which is taken as equal to the seismogram duration. We use $T = 24$ hr and exponent $\nu = 1$. Phase correlation provides a measure of the similarity of the two time-series as a function of lag time τ, which is unbiased by the amplitude of the two signals. This strategy allows the detection of weak amplitude signals that are more phase-coherent than noise and therefore can be more efficient than using the classical approach.

Daily cross-correlograms between each station pair are then stacked non-linearly using the time–frequency phase-weighted stack method (Schimmel & Gallart 2007; Schimmel *et al.* 2011). For each day j, we compute the S-transform of the cross-correlogram, $C_{\mathrm{pcc}_j}(\tau)$, to obtain its time–frequency representation, $S_j(\tau, f) = ST(C_{\mathrm{pcc}_j}(\tau))$ (Stockwell *et al.* 1996). The corresponding time–frequency instantaneous phase is defined as $\frac{S_j(\tau,f)e^{i2\pi f\tau}}{|S_j(\tau,f)|}$. We compute the time–frequency phase-weighted stack as the product of the time–frequency phase stack and the S-transform of the linear stack of the daily correlograms:

$$S_{\mathrm{pws}}(\tau, f) = \left|\frac{1}{N}\sum_{j=1}^{N}\frac{S_j(\tau, f)e^{i2\pi f\tau}}{|S_j(\tau, f)|}\right|^{\nu} .ST\left(\frac{1}{N}\sum_{i=1}^{N}C_{\mathrm{PCC}_i}(\tau)\right) \quad (2)$$

where N is the number of daily phase correlograms. We use the exponent $\nu = 2$ and we stack together correlograms for positive and negative lag times after time-reversing negative time lags. Finally, we compute the inverse of the S-transform (Schimmel & Paulssen 1997; Schimmel & Gallart 2005) to obtain the stack $s_{\mathrm{pws}}(\tau)$ as a function of the time lag τ. For more details on this method, the reader is addressed to Schimmel & Gallart (2007) and Schimmel *et al.* (2011). In this approach, the time–frequency-dependent phase coherence is used as a data adaptive attribute to attenuate the incoherent noise. The benefits are that coherent signals stand out more clearly with respect to the incoherent noise.

2.2 Robust group-velocity measurement

To perform a global study of the Earth upper mantle, we measure Rayleigh wave group velocities in the frequency band of 0.004–0.032 Hz. The group velocity corresponds to the maximum energy as a function of the frequency of the EGF time–frequency representation $S_{\mathrm{pws}}(\tau, f)$. The highest frequency is fixed at 0.032 Hz for all station pairs and the lowest frequency is adjusted so that the interstation distance corresponds to at least three wavelengths. Station pairs with interstation distances ranging from 500 to 15 000 km are selected.

2.2.1 Convergence of the group-velocity measurement

One parameter to adjust is the amount of data to stack to obtain reliable group-velocity measurements. We first used 1 yr of data recorded by the vertical component of broad-band stations. We filtered the data between 0.003 and 0.020 Hz, and we applied the PCPWS method. Fig. 1 shows an example of the EGF that corresponds to the path between two GEOSCOPE stations, as INU in Japan and CLF in France. The interstation distance is 9738 km. Fig. 1(a) shows that we can clearly identify the R1 and R2 trains of Rayleigh waves. We then compute the S-transform of the R1 arc Rayleigh waves (between the dashed lines in Fig. 1a) and Fig. 1(c) shows the energy diagram normalized per frequency. The group velocity can be measured in the entire frequency band of 0.003–0.020 Hz without ambiguity (Fig. 1c, green line). This group velocity is hereafter called the reference group velocity, V_{ref}.

We then evaluated the convergence towards V_{ref} as a function of the frequency and the amount of stacked data. We randomly selected a subset of phase correlograms that correspond to a fixed number of days, and we measured the group velocity from their phase-weighted stack. We repeated the measurement 20 times on different random subdata sets, and we computed the median group velocity V_{med}. Fig. 1(e) shows the relative difference between V_{ref} and V_{med} for each frequency and number of days. We see that at

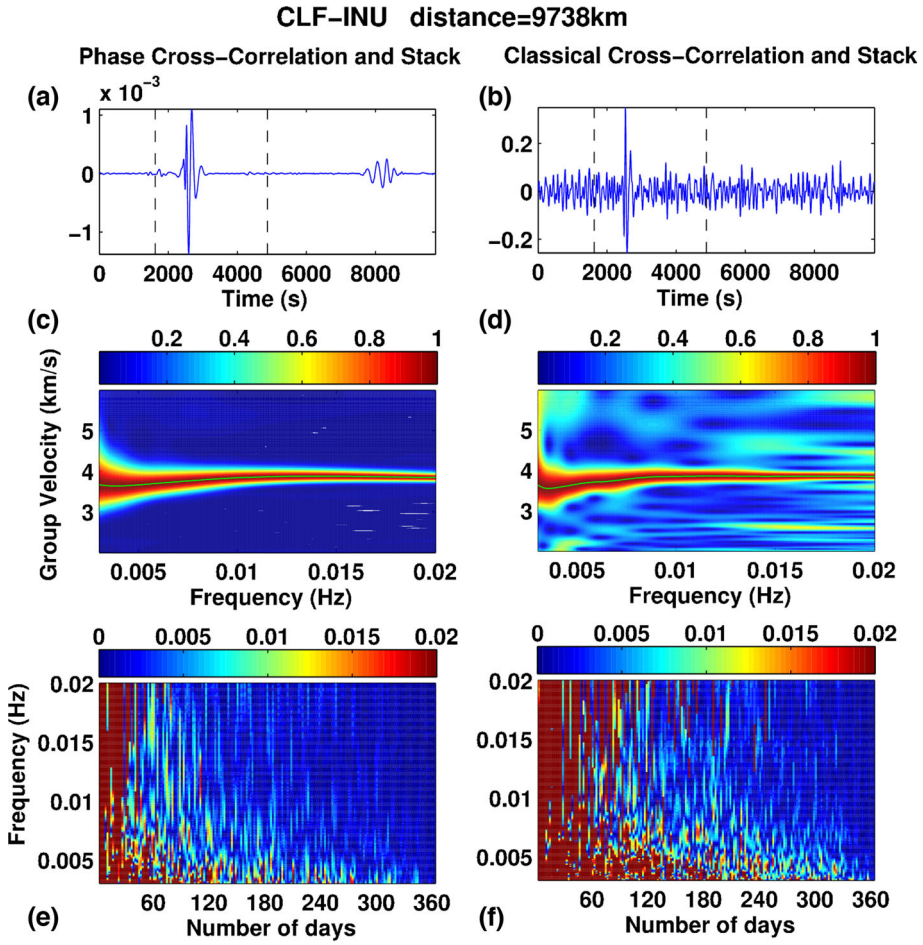

Figure 1. EGFs obtained from 1 yr of noise recorded by stations CLF (France) and INU (Japan) from the GEOSCOPE network, using the PCPWS method (a) and the CCS method (b). In (a), minor and major arc Rayleigh waves can be clearly identified, whereas in (b) the signal-to-noise ratio is lower and only the minor arc Rayleigh wave is visible. The energy diagrams in (c) and (d) are those for the EGFs plotted in (a) and (b), respectively. The measured group velocity is in green. (e) and (f) show the relative differences with respect to the reference group velocities, in green in (c) and (d), respectively, as a function of frequency and number of days stacked. Both methods require more data to be stacked to recover group velocities at long periods than at short periods. The reference group velocity (dark blue) is accurately recovered after stacking fewer days using the PCPWS method (e), than the CCS method (f).

high frequencies (i.e. 0.02–0.01 Hz) the reference group velocity is retrieved after stacking about 120 d, whereas at long periods (i.e. 0.005 Hz), about 320 d are necessary to converge toward V_{ref}.

For comparison, we also evaluated the convergence towards the reference group velocity using classical data processing, here referred to as the CCS method (Bensen *et al.* 2007). Data were cut into 24-hr segments, filtered between 0.003 and 0.020 Hz and normalized to 1 bit. We then applied spectral whitening and computed the classical correlation between the daily traces. Correlograms were linearly stacked. Fig. 1(b) shows that the EGF computed with the CCS method is noisier than the EGF computed with the PCPWS method (Fig. 1a). We can still identify the R1 Rayleigh wave train, but the R2 train is not visible. Nevertheless, the R1 train group velocity, V_{CCSref}, can be accurately measured (Fig. 1d), even though the energy diagram is noisier than in Fig. 1(c). Finally, we analysed the convergence toward V_{CCSref}. Fig. 1(f) shows that the convergence is slower than with the PCPSW method. We need to stack at least 250 d at short periods and at least 1 yr of data at long periods to converge toward V_{CCSref}. We similarly investigated many station pairs for varying epicentral distances, and concluded that the PCPWS method provides less noisy EGF and group-velocity measurements in the wide frequency band of interest than the CCS method. In the following, we have only used the PCPWS method.

2.2.2 Selection of the frequency range and the amount of data

We then tested the robustness of the group-velocity measurement by comparing the measurements on the positive, negative and symmetric EGFs. Fig. 2(a) shows the EGFs for positive and negative time lags and Fig. 2(b) shows the EGFs after the phase-weighted stack of all of the positive and reversed negative phase correlograms together. In all three cases, the Rayleigh waveform is clearly visible. Fig. 2(c) shows the group velocities corresponding to the three EGFs. We obtain the same group velocities between 30 and 180 s of the periods, but the group velocities are different at longer periods. We then added another 1 yr of data, and so stacked these 2 yr of data. Figs 2(d) and (e) show almost no differences with respect to the EGF in Figs 2(a) and (b), although Fig. 2(f) shows that the group velocities of the positive, negative and symmetric correlograms are now similar for the entire period band. Therefore, in the following we stacked together 2 yr of data with positive and reversed-negative time lags.

Even after stacking 2 yr of data, we often observed that the group velocity could not be recovered in the entire frequency band. This is illustrated in Figs 3(a) and (b) for the path between station BKNI in Indonesia and PET in Russia. The interstation distance is 7879 km. Fig. 3(a) shows that the waveform is complex, and Fig. 3(b)

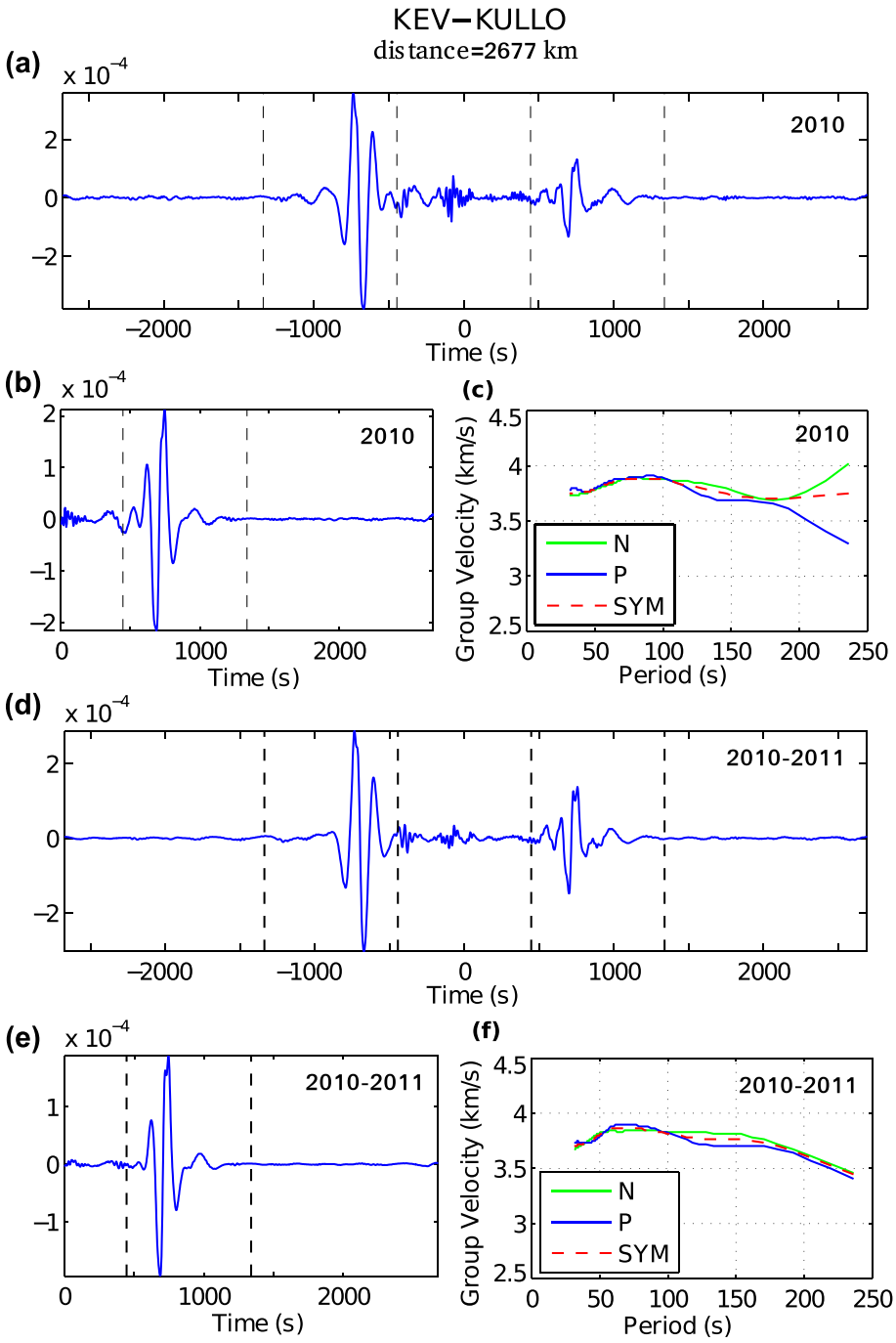

Figure 2. (a) EGF obtained using the PCPWS method on 1 yr (2010) of noise recorded by stations KEV (IU network, Finland) and KULLO (DK/GLISN network, Greenland). (b) EGF (SYM) obtained after phase-weighted stacking positive and reversed negative time-lag phase correlograms. (c) Group velocities measured using the EGF in (a) with positive time (blue), with reversed negative time (green), and the EGF in (b) (red). The three group-velocity curves differ for periods larger than 170 s. (d)–(f) The same as for (a)–(c), but obtained after stacking 2 yr of data. The group velocities measured on the EGF of positive, reversed negative and symmetric times are similar across the entire period band.

suggests that the group velocity can only be measured between 0.014 and 0.030 Hz. We then filtered the raw data in two frequency bands of 0.004–0.016 Hz and 0.016–0.032 Hz, and we processed the data in the two frequency bands separately. Figs 3(c) and (d) show that the signal-to-noise ratio is much higher in each frequency band, both for the correlograms and for the group velocities. In the following, we therefore processed the data in the two frequency bands separately.

2.2.3 *Group-velocity automatic selection and error estimation*

To select reliable group velocities as a function of frequency as automatically as possible, we used the statistical approach of Schimmel *et al.* (2015). For each interstation path, the reference group velocity, V_{ref}, is measured from the EGF obtained from the stack of 2 yr of data. We then randomly select 20 subsets of data corresponding to 70 per cent of the total data. For each subset, the group velocity

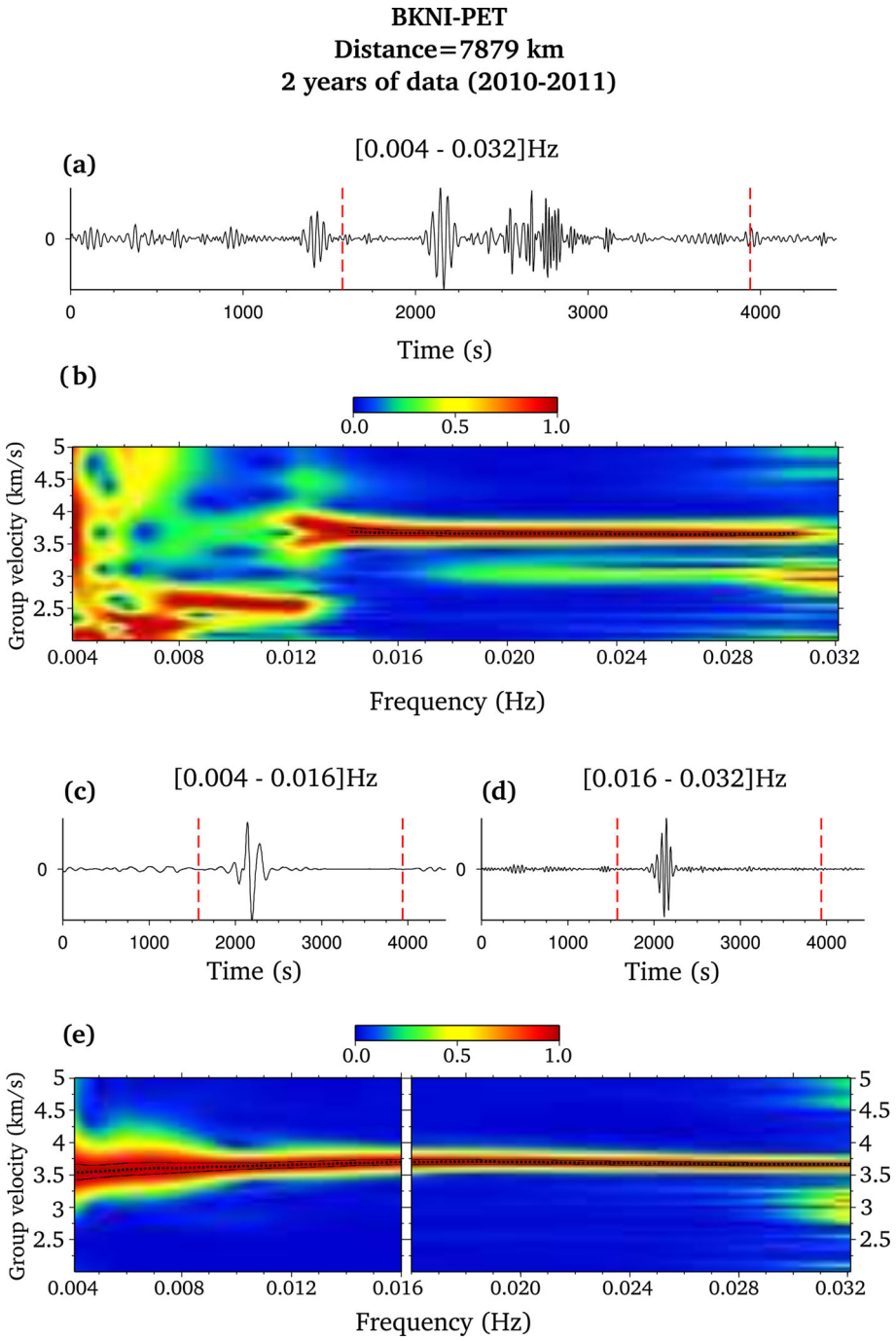

Figure 3. (a) EGF obtained in the frequency band of 0.004–0.032 Hz using the PCPWS method on 2 yr (2010–2011) of noise recorded by station BKNI (GE network, Indonesia) and PET (IU network, Russia). (b) Energy diagram computed for the Rayleigh wave train between the dashed red lines in (a). The group velocity can be measured only between 0.014 and 0.030 Hz (black line and error bars). (c) and (d) show the EGF computed on filtered data in the frequency band of 0.004–0.016 Hz and 0.016–0.032 Hz, respectively. (e) Corresponding energy diagrams. The group velocity can be measured without ambiguity across the entire frequency range.

is measured and compared to V_{ref}. We only keep group velocities in the frequency range where at least 75 per cent of the measurements are consistent.

In the frequency range of accurate measurement, the measurement error depends on the sharpness of the S-transform maximum as a function of frequency. Therefore, the error associated with each measurement is set to correspond to 95 per cent of the normalized maximum amplitude at each frequency. This approximates empirically the frequency-dependent uncertainty of the group velocity maximum, which is plotted in Figs 3(b) and (e) as the black lines around the maximum.

3 DATA

We selected stations from the global networks of GEOSCOPE (G), GSN (IU, II) and GEOFON (GE). We also added some stations from the MEDNET, CDSN and Algerian (ADSN) networks to complete

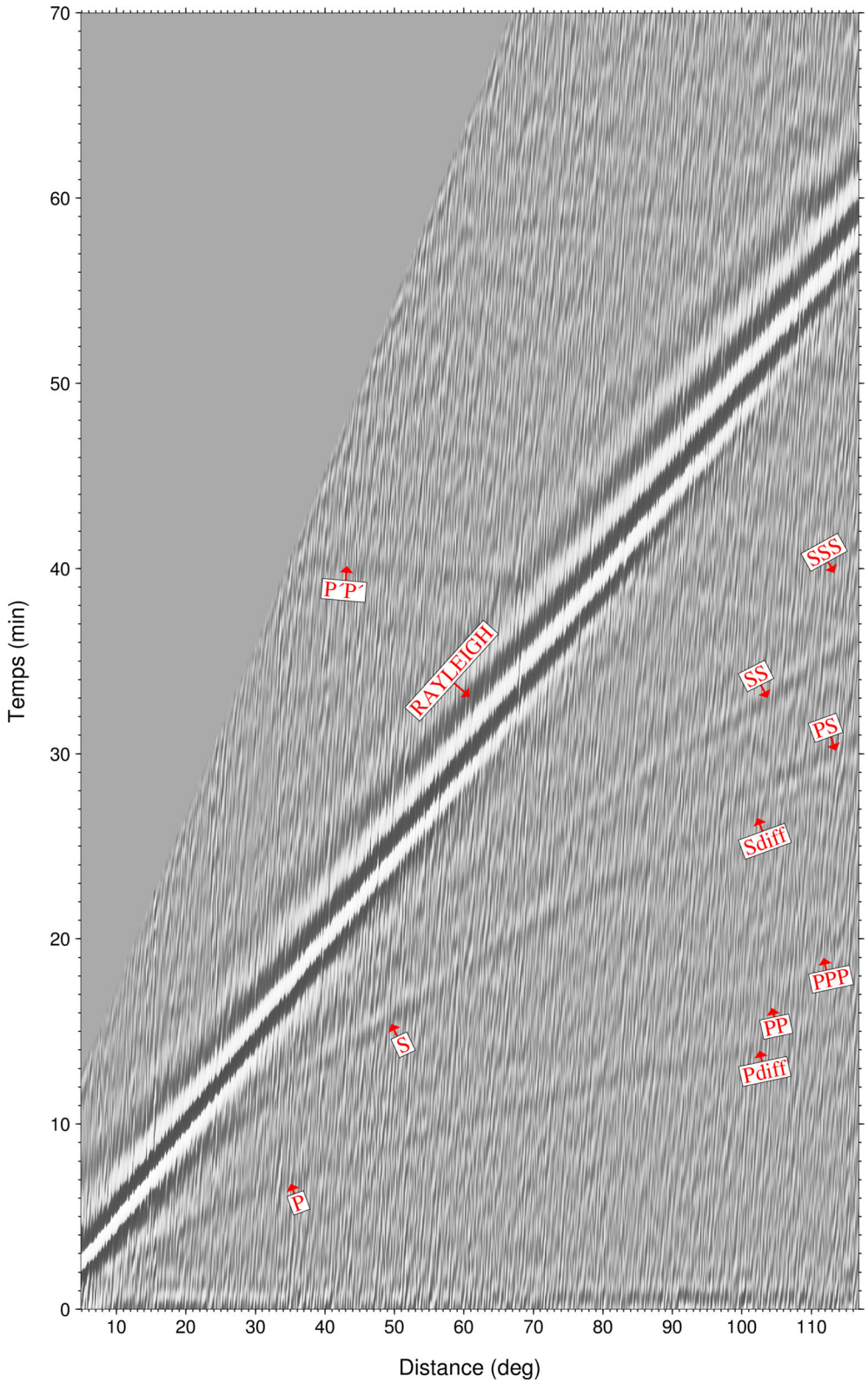

Figure 4. EGFs as a function of distance and time. Rayleigh waves and body waves with a high signal-to-noise ratios are clearly visible.

the global Earth coverage. The first selection of the stations was performed to remove stations with instrumental problems. In total, we used 2 yr (2010–2011) of data from 149 stations that corresponds to 8440 paths with interstation distances between 500 and 13000 km. We applied the automatic PCPWS method, and also checked each measurement manually. We obtained reliable group-velocity measurements along 6797 paths, which corresponded to 80 per cent of the paths.

Fig. 4 shows the EGF as a function of distance in the frequency range of 0.004–0.016 Hz, and we can clearly identify the Rayleigh

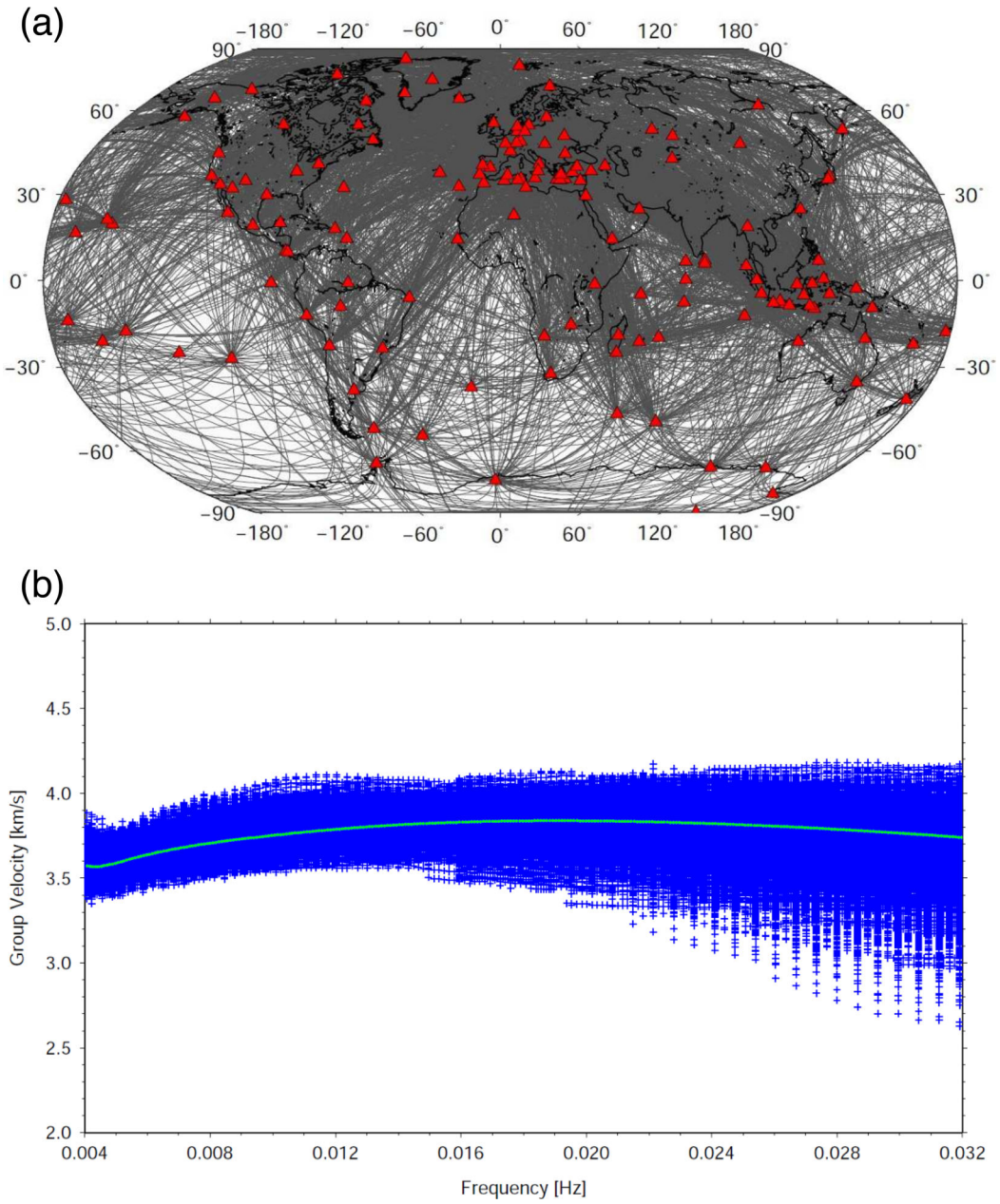

Figure 5. (a) Geographical map with the stations (red triangles) and interstation paths (grey lines) used in the inversion. (b) Group-velocity measurements (blue) as a function of frequency. The PREM group velocity is plotted for comparison (green).

wave train with a high signal-to-noise ratio. We can also identify several body-wave phases. Body waves have been previously observed on noise EGFs at short distances and high frequencies (e.g. Schimmel *et al.* 2011). They were also observed at teleseismic distances by Nishida (2013), who stacked 8 yr of data filtered between 5 and 40 mHz recorded by 650 stations, and by Boué *et al.* (2013), who used 1 yr of data recorded by 339 stations and filtered data in the period band of 10–40 mHz. Nevertheless, these observations are still rare. Here, body waves are clearly visible on the hodochrones obtained by plotting the 6797 EGFs binned over 20 km in distance and 3 s in time, and without further pre-processing. These body waves are not used in this study, but they are clearly visible due to the high signal-to-noise ratio of our EGFs.

Fig. 5(a) shows the station locations and path distributions and Fig. 5(b) shows the 6797 measured group velocities as a function of frequency. The preliminary reference earth model (PREM) group velocity is plotted for comparison, and it can be seen that our global group velocities cluster around the average model. We observe that the group-velocity variability is larger at short periods than at long periods, which is expected because the strong lateral heterogeneities in the crust mostly affect short-period group velocities. We then selected 12 frequencies to describe the entire frequency range, and we obtained a set of 81 564 group-velocity measurements.

4 TOMOGRAPHIC MODEL

We followed the classical approach in surface wave tomography to build the 3-D model of the *S*-wave velocity in two steps but an original trans-dimensional inversion scheme is used in the second

step. The first step, called regionalisation, inverts the path average group velocities to obtain 2-D maps of local group velocities. This is applied to data sets that separately correspond to each period. The second step combines the group-velocity maps corresponding to different periods and inverts them separately at each gridpoint, to obtain the local *S*-wave velocity as a function of depth. These local models are then recombined to obtain the 3-D *S*-wave velocity model.

4.1 Group-velocity maps

We apply here the method of Montagner (1986), which uses smooth local basis functions and the continuous inverse formalism of Tarantola & Valette (1982) to obtain local group velocities. The *a-priori* group-velocity error and correlation length between neighbouring points are introduced through a Gaussian *a-priori* covariance function. Both *a-priori* parameters are determined empirically by considering simultaneously the variance reduction and χ^2 criteria (e.g. Sebai *et al.* 2006), and we selected a correlation length of 800 km and *a-priori* model error of 0.1 km s^{-1}. We used the code of Debayle & Sambridge (2004), which proposes efficient parametrisation of the model based on Voronoi cells, and enables the optimisation of the matrix sizes as a function of the path coverage. The forward problem computes great-circle arcs to trace the rays along the interstation paths.

The *a-posteriori* errors on the group-velocity maps, which depend on the measurement quality and the path coverage, are computed using the *a-posteriori* covariance matrix (Tarantola & Nercessian 1984), and they are used for the group-velocity inversion *versus* depth. We also estimated the resolution of the group-velocity maps with synthetic tests (Appendix A). Anomalies of 2000 km width are well recovered between latitudes of 72°N and 54°S, and anomalies of 3000 km width are well recovered between latitudes of 81°N and 54°S. At higher latitudes, the resolution decreases due to the lack of stations.

Fig. 6 shows the group-velocity perturbation maps for the four periods of 30, 100, 170 and 235 s that are obtained from the interstation measurements of Fig. 5. We observe large velocity variations at short periods, and smaller variations at longer periods. At the short period (i.e. 30 s), we clearly see the ocean–continent difference, with slower velocity beneath continents and faster velocity beneath oceans. These variations are related to the difference in the crustal thickness between oceans and continents. Indeed, the continental crust is thicker than the global average crust, and therefore short-period group-velocity perturbations are slower beneath continents. At the 100-s period, we observe fast velocities beneath cratons and slow velocities beneath ridges. These features persist at the longer period (i.e. 170 s), although the velocity anomaly amplitude decreases, such that at the 235 s period, the correlation with surface tectonics disappears. Large-scale structures obtained in this study are consistent with the group-velocity maps obtained from earthquake surface wave data (e.g. Ekström 2011).The Pearson correlation (eq. A1) between these two models is between 0.80 and 0.85 in the period range of 40–200 s.

4.2 *S*-wave velocity model

The global group-velocity maps and corresponding uncertainties are then inverted to obtain the tomographic *S*-wave velocity model. We use a trans-dimensional inversion technique, which automatically adapts the model parametrization to the group-velocity uncertainty (e.g. Sambridge *et al.* 2013). The inversion is performed for each location on a grid of $2^\circ \times 2^\circ$ in latitude and longitude. The *a-priori* earth model is composed of the local crust1.0 model (Laske *et al.* 2013) and the PREM model, where the 220 km discontinuity is smoothed. We checked that when crust2.0 or crust1.0 are used, the model does not change our tomographic images significantly. The trans-dimensional inversion is a composition of two nested loops: the inner loop computes for a given spline basis the optimum model weight coefficients and the outer loop determines the optimum spline basis. The inversion scheme is presented in Appendix B.

To determine the resolution of the inversion *versus* depth, synthetic tests are presented in Appendix A. These show that two delta-like anomalies (positive or negative) separated by 90 km are recovered in the depth range of 50–250 km. The inverted model smoothing effect increases with depth due to the different sensitivity of the Rayleigh wave fundamental mode with depth.

S-wave velocity maps are shown in Fig. 7 for the selected depths of 80, 140 and 200 km. This model is hereafter called the HUM2 model. At shallow depth, the model correlates well with surface tectonics; that is, at 80 km in depth, the mid-ocean ridges have slow signatures, whereas the cratons and thick lithosphere are associated with fast anomalies. The island of Madagascar is clearly identified as a shallow fast anomaly structure that disappears at 140 km. At 140 km depth, slow anomalies beneath oceans become more uniform as they correspond to the asthenosphere. At this depth, cratons beneath all of the continents are still visible as fast anomalies, except beneath India where the Dharwar craton fast signature has disappeared.

Fig. 8 shows that the Dharwar craton is less than 100 km thick, which is consistent with receiver function results (Kumar *et al.* 2007). For comparison, the West African craton is faster than the PREM model, at least down to 200 km. Beneath the Afar plume (Fig. 8), we resolve a strong slow anomaly that is visible down to at least 200 km in depth as expected for a deep plume origin (Davaille *et al.* 2005). In comparison, the slow anomaly beneath the Cape Verde plume is much weaker and in agreement with the joint seismic-geodynamic model (Forte *et al.* 2010), and also with Davaille *et al.* (2005), who suggested that Cape Verde is a small secondary plume that originated 30–40 Ma ago at the top of a large thermochemical plume that was visible from the bottom of the mantle to the transition zone.

4.3 Discussion

We compared our HUM2 model with three published global models: the model from Nishida *et al.* (2009), which is the only other model that was derived solely from hum data (hereafter called NMK2009), and two global models derived from earthquake data: model DR2012 from Debayle & Ricard (2012) and model SAVANI from Auer *et al.* (2014). For more details, the reader is addressed to Appendix A2. The Pearson correlation between our HUM2 model and the NMK2009 model is only about 0.65 in the depth range of 70–280 km, and it decreases at shallower depth, down to 0.40 (Fig. A2). This low correlation is also observed between the models NMK2009 and DR2012 or SAVANI, and can be explained in two ways. First, the NMK2009 model is derived from limited data, and therefore its lateral resolution is lower than for the other models. Then, they used long period hum data (periods larger than 110 s), which cannot resolve shallow structures.

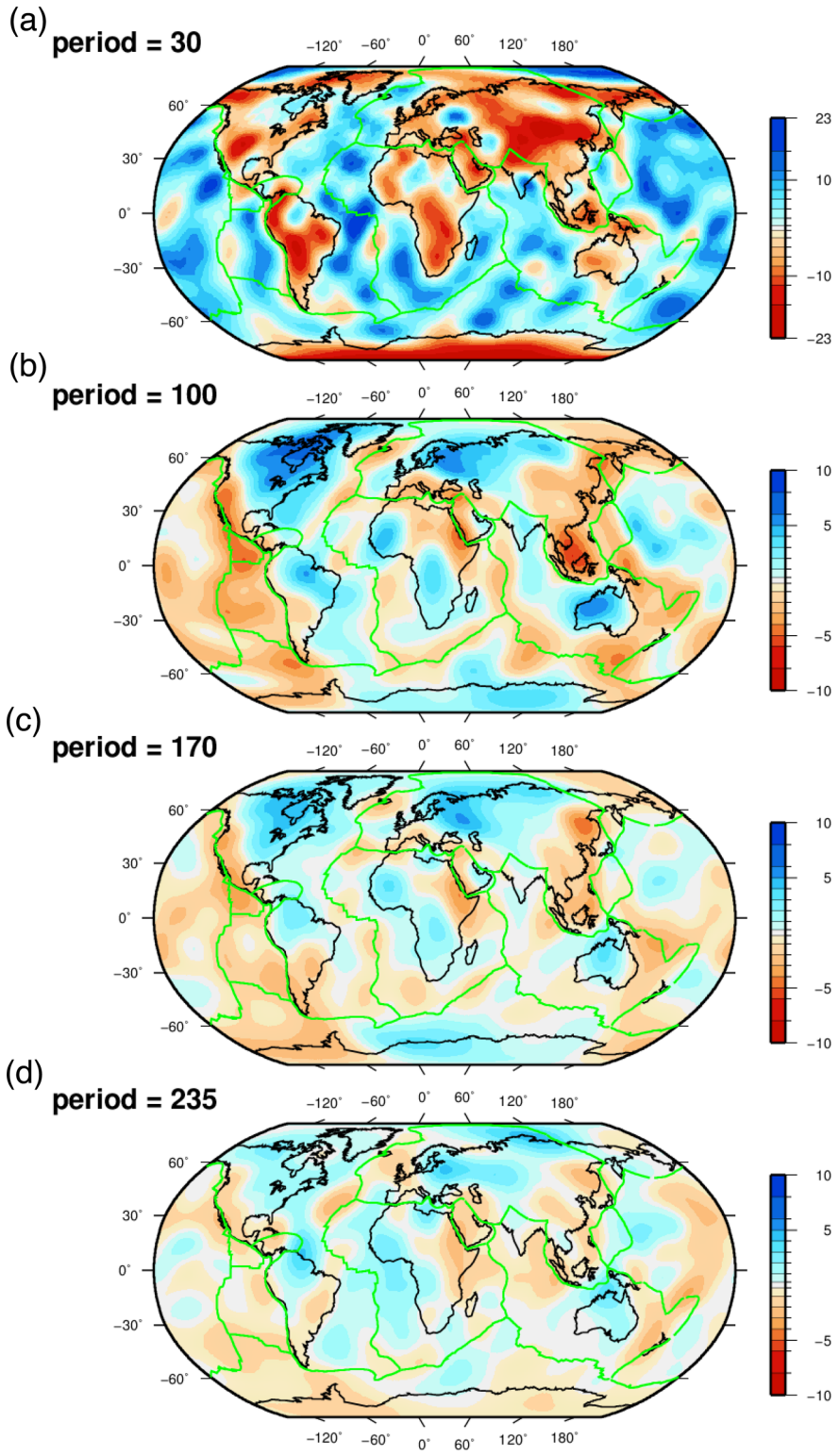

Figure 6. Group-velocity maps for periods of 30 s (a), 100 s (b), 170 s (c) and 235 s (d).

Correlation between our HUM2 model and the DR2012 or SAVANI models is much higher, at about 0.90, between 70 and 200 km in depth (Fig. A2). This high correlation can be confirmed by visual comparisons of the models, and their large-scale structures are similar for all three models. Nevertheless, in some areas, such as the subduction zone beneath South America, the HUM2 model has poorer resolution, due to the limited number of stations used in that area. This area is better resolved by the two other models, due to the large numbers of subduction earthquakes. On the other hand, features such as the island of Madagascar or the east European craton, are better resolved by the HUM2 model due to the different path coverage of our model (Fig. 7), which

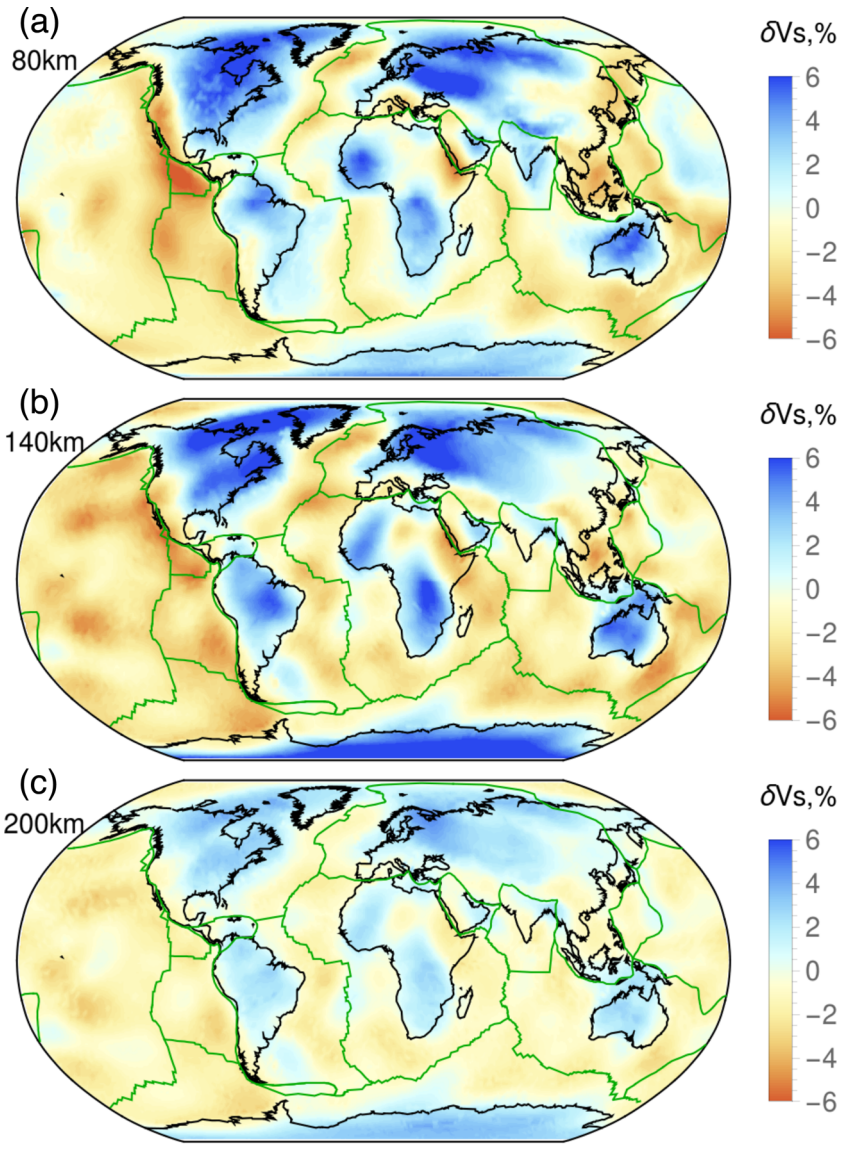

Figure 7. *S*-wave velocity maps at 80, 140 and 200 km in depth. Velocity perturbations are in per cent with respect to the average model shown in Fig. 8.

is only related to station locations and not to station-earthquake locations.

At shallow depths ($\leq$70 km), the correlation with the SAVANI model remains high (0.70–0.75), although correlation with the DR2012 model decreases down to 0.40. At shallow depths, the main difference between these models is related to the shallow-layer correction. All three models use crust2.0 or crust1.0 shallow models, and the main issue is how crustal correction is implemented. In this study, the crust1.0 model is horizontally smoothed and used as the *a-priori* model in each gridpoint, without being inverted. Then, beneath Tibet, where the crust thickness is 75 km in the crust1.0 model, our model shows a fast mantle anomaly at 80 km in depth, whereas the DR2012 and SAVANI models show slow anomalies. Their slow anomalies are related to the vertical smoothing of the crust. Deeper than 140 and 200 km in depth, all three of the models show a fast anomaly beneath Tibet.

We also compared the models at the four locations shown in Fig. 8. All four of these models show consistent fast anomalies beneath cratons and slow anomalies beneath hotspots. But the amplitudes and depths of the velocity anomaly differ (Fig. A3). For example, in West Africa, the HUM2 model is similar to the SAVANI model between 50 and 100 km in depth and closer to the deeper DR2012. Beneath Dharwar craton, the minimum velocity is shallower (about 150 km) in model HUM2 than in models SAVANI and DR2012, where it is close to 200 km.

Despite some of the differences discussed above, the high correlation between tomographic models derived from earthquake and noise data confirms that hum data can provide accurate information on the earth structure. Earthquake and hum data provide different path coverage, and therefore they are complementary data sets and they should be inverted jointly to improve the Earth models.

5 CONCLUSIONS

We applied the new PCPWS method based on the analytical signal developed by Schimmel *et al.* (2011) to derive a new global tomographic model of the upper mantle from the hum recorded worldwide in the period band 30–250 s.

We first computed the phase correlograms between station pairs to extract the phase-coherent signals. We stacked the correlograms

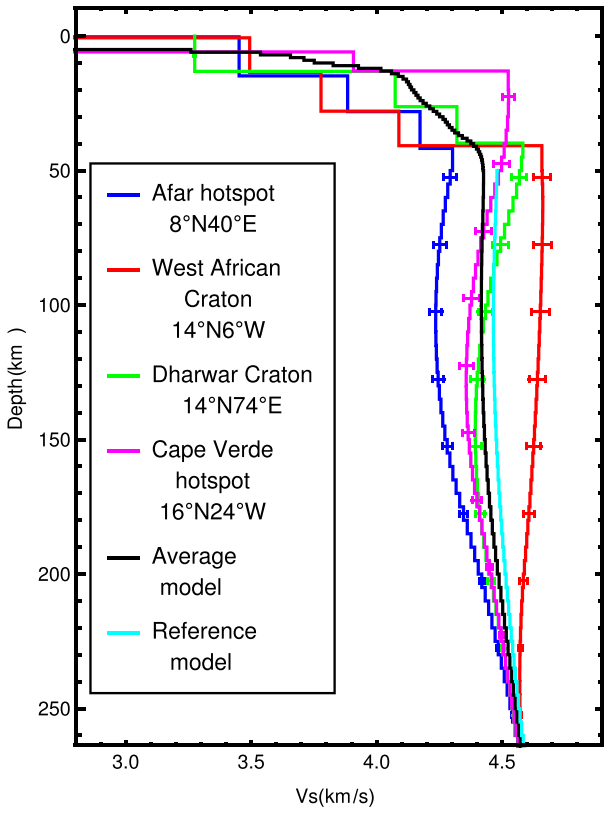

Figure 8. *S*-wave velocity as a function of depth for two cratons (red, West Africa; green, Dharwar) and two hotspots (blue, Afar, purple, Cape Verde). The *a-priori* reference model is plotted in light blue and the global averages model obtained after inversion is plotted in black.

using the time–frequency phase-weighted stack method to build-up the EGFs. Group velocities were then automatically computed using a resampling method to select robust measurements. We tested the stability of the group-velocity measurements as a function of the amount of stacked data and the frequency. Less data are required at high frequency than at low frequency, and it is necessary to stack 2 yr of hum to obtain robust measurements in the entire frequency band of 0.004–0.032 Hz. We further show that it is necessary to process data in separate frequency bands, as 0.004–0.016 Hz and 0.016–0.032 Hz, to obtain reliable group-velocity measurements in the entire frequency band. Comparing the PCPWS (Schimmel *et al.* 2011) and CCS (Bensen *et al.* 2007) methods, we show that the PCPWS method enables faster convergence towards higher signal-to-noise ratio EGFs.

We selected 149 good-quality broad-band stations from the global networks and obtained 6797 group-velocity curves that corresponded to paths between 500 and 13000 km. We only rejected measurements along 20 per cent of the paths for which no convergence toward the EGF could be achieved. The selected EGFs show high signal-to-noise ratios, and both Rayleigh waves and body waves can be clearly identified.

The group velocities were regionalized and then inverted, to obtain the 3-D *S*-wave velocity model using a simulated annealing method in which the number and shape of the splines that describe the model vary. This new *S*-wave velocity tomographic model is well correlated with models derived from earthquakes in most areas, although in India, the Dharwar craton is shallower than in other published models.

This model will be improved in the future by using more stations, and in particular, ocean-bottom stations. Earthquakes and ambient noise provide independent data sets and path coverage, and therefore are complementary to investigate the structure of the Earth.

ACKNOWLEDGEMENTS

This is IPGP contribution number 3700. Numerical computations were performed on the S-CAPAD platform, IPGP, France. M.S. acknowledges the Spanish MISTERIOS project CGL2013-48601-C2-1-R.

REFERENCES

Ardhuin, F., Stutzmann, E., Schimmel, M. & Mangeney, A., 2011. Ocean wave sources of seismic noise, *J. geophys. Res.,* **116,** C09004, doi:10.1029/2011JC006952.

Ardhuin, F., Gualtieri, L. & Stutzmann, E., 2015. How ocean waves rock the earth: two mechanisms explain microseisms with periods 3 to 300 s, *Geophys. Res. Lett.,* **42**(3), 765–772.

Auer, L., Boschi, L., Becker, T., Nissen-Meyer, T. & Giardini, D., 2014. Savani: a variable resolution whole-mantle model of anisotropic shear velocity variations based on multiple data sets, *J. geophys. Res.,* **119**(4), 3006–3034.

Bensen, G., Ritzwoller, M., Barmin, M., Levshin, A., Lin, F., Moschetti, M., Shapiro, N. & Yang, Y., 2007. Processing seismic ambient noise data to obtain reliable broad-band surface wave dispersion measurements, *Geophys. J. Int.,* **169**(3), 1239–1260.

Bensen, G., Ritzwoller, M. & Shapiro, N., 2008. Broadband ambient noise surface wave tomography across the United States, *J. geophys. Res.,* **113,** B05306, doi:10.1029/2007JB005248.

Biswas, N. & Knopoff, L., 1970. Exact earth-flattening calculation for love waves, *Bull. seism. Soc. Am.,* **60**(4), 1123–1137.

Boué, P., Poli, P., Campillo, M., Pedersen, H., Briand, X. & Roux, P., 2013. Teleseismic correlations of ambient seismic noise for deep global imaging of the earth, *Geophys. J. Int.,* **194**(2), 844–848.

Davaille, A., Stutzmann, E., Silveira, G., Besse, J. & Courtillot, V., 2005. Convective patterns under the Indo-Atlantic box, *Earth planet. Sci. Lett.,* **239**(3), 233–252.

De Boor, C., 1978. *A Practical Guide to Splines: Applied Mathematical Sciences,* Vol. 27, pp. 109–112, Springer-Verlag.

Debayle, E. & Ricard, Y., 2012. A global shear velocity model of the upper mantle from fundamental and higher Rayleigh mode measurements, *J. geophys. Res.,* **117,** B10308, doi:10.1029/2012JB009288.

Debayle, E. & Sambridge, M., 2004. Inversion of massive surface wave data sets: model construction and resolution assessment, *J. geophys. Res.,* **109,** B02316, doi:10.1029/2003JB002652.

Derode, A., Larose, E., Tanter, M., De Rosny, J., Tourin, A., Campillo, M. & Fink, M., 2003. Recovering the Green's function from field-field correlations in an open scattering medium (L), *J. acoust. Soc. Am.,* **113**(6), 2973–2976.

Dias, R.C., Julià, J. & Schimmel, M., 2015. Rayleigh-wave, group-velocity tomography of the Borborema Province, NE Brazil, from ambient seismic noise, *Pure appl. Geophys.,* **172**(6), 1429–1449.

Dziewonski, A.M. & Anderson, D.L., 1981. Preliminary reference earth model, *Phys. Earth planet. Inter.,* **25**(4), 297–356.

Ekström, G., 2011. A global model of Love and Rayleigh surface wave dispersion and anisotropy, 25–250 s, *Geophys. J. Int.,* **187**(3), 1668–1686.

Forte, A.M., Quéré, S., Moucha, R., Simmons, N.A., Grand, S.P., Mitrovica, J.X. & Rowley, D.B., 2010. Joint seismic–geodynamic-mineral physical modelling of African geodynamics: a reconciliation of deep-mantle convection with surface geophysical constraints, *Earth planet. Sci. Lett.,* **295**(3), 329–341.

Hasselmann, K., 1963. A statistical analysis of the generation of microseisms, *Rev. Geophys.,* **1**(2), 177–210.

Kedar, S., Longuet-Higgins, M., Webb, F., Graham, N., Clayton, R. & Jones, C., 2008. The origin of deep ocean microseisms in the North Atlantic Ocean, *Proc. R. Soc. A: Math. Phys. Eng. Sci.,* **464**(2091), 777–793.

Kumar, P., Yuan, X., Kumar, M.R., Kind, R., Li, X. & Chadha, R., 2007. The rapid drift of the Indian tectonic plate, *Nature,* **449**(7164), 894–897.

Laske, G., Masters, G., Ma, Z. & Pasyanos, M., 2013. Update on CRUST1.0 – a 1-degree global model of Earth's crust, in *Geophysical Research Abstracts,* vol. 15, p. 2658.

Lobkis, O. & Weaver, R., 2001. On the emergence of the Green's function in the correlations of a diffuse field, *J. acoust. Soc. Am.,* **110**(6), 3011–3017.

Longuet-Higgins, M.S., 1950. A theory of the origin of microseisms, *Phil. Trans. R. Soc. Lond., A. Math. Phys. Sci.,* **243**(857), 1–35.

Menke, W., 2012. *Geophysical Data Analysis: Discrete Inverse Theory,* Academic press.

Montagner, J.-P., 1986. Regional three-dimensional structures using long-period surface waves, *Ann. Geophys. Terr. Planet. Phys.,* **4,** 283–294.

Moulik, P. & Ekström, G., 2014. An anisotropic shear velocity model of the Earth's mantle using normal modes, body waves, surface waves and long-period waveforms, *Geophys. J. Int.,* **199**(3), 1713–1738.

Nishida, K., 2013. Earth's background free oscillations, *Ann. Rev. Earth Planet. Sci.,* **41,** 719–740.

Nishida, K., Montagner, J.-P. & Kawakatsu, H., 2009. Global surface wave tomography using seismic hum, *Science,* **326**(5949), 112, doi:10.1126/science1176389.

Press, W.H., 2007. *Numerical Recipes 3rd Edition: The Art of Scientific Computing,* Cambridge Univ. Press.

Rhie, J. & Romanowicz, B., 2004. Excitation of Earth's continuous free oscillations by atmosphere–ocean–seafloor coupling, *Nature,* **431**(7008), 552–556.

Sabra, K.G., Gerstoft, P., Roux, P., Kuperman, W. & Fehler, M.C., 2005. Surface wave tomography from microseisms in Southern California, *Geophys. Res. Lett.,* **32,** L14311, doi:10.1029/2005GL023155.

Saito, M., 1988. DISPER80: a subroutine package for the calculation of seismic normal-mode solutions, in *Seismological Algorithms,* pp. 293–319, ed. Doornbos, D.J., Academic Press, New York.

Sambridge, M., Bodin, T., Gallagher, K. & Tkalčić, H., 2013. Transdimensional inference in the geosciences, *Phil. Trans. R. Soc. Lond., A.: Math. Phys. Eng. Sci.,* **371**(1984), 20110547, doi:10.1098/rsta.2011.0547.

Schimmel, M., 1999. Phase cross-correlations: design, comparisons, and applications, *Bull. seism. Soc. Am.,* **89**(5), 1366–1378.

Schimmel, M. & Gallart, J., 2005. The inverse S-transform in filters with time-frequency localization, *IEEE Trans. Signal Process.,* **53**(11), 4417–4422.

Schimmel, M. & Gallart, J., 2007. Frequency-dependent phase coherence for noise suppression in seismic array data, *J. geophys. Res.,* **112,** B04303, doi:10.1029/2006JB004680.

Schimmel, M. & Paulssen, H., 1997. Noise reduction and detection of weak, coherent signals through phase-weighted stacks, *Geophys. J. Int.,* **130**(2), 497–505.

Schimmel, M., Stutzmann, E. & Gallart, J., 2011. Using instantaneous phase coherence for signal extraction from ambient noise data at a local to a global scale, *Geophys. J. Int.,* **184**(1), 494–506.

Schimmel, M., Stutzmann, E. & Ventosa, S., 2015. Robust group velocity measurements, *IEEE,* submitted.

Sebai, A., Stutzmann, E., Montagner, J.-P., Sicilia, D. & Beucler, E., 2006. Anisotropic structure of the African upper mantle from Rayleigh and Love wave tomography, *Phys. Earth planet. Inter.,* **155**(1), 48–62.

Shapiro, N.M., Campillo, M., Stehly, L. & Ritzwoller, M.H., 2005. High-resolution surface-wave tomography from ambient seismic noise, *Science,* **307**(5715), 1615–1618.

Snieder, R., 2004. Extracting the Green's function from the correlation of coda waves: a derivation based on stationary phase, *Phys. Rev. E,* **69**(4), doi:10.1103/PhysRevE.69.046610.

Stockwell, R.G., Mansinha, L. & Lowe, R., 1996. Localization of the complex spectrum: the S transform, *IEEE Trans. Signal Process.,* **44**(4), 998–1001.

Stutzmann, E., Ardhuin, F., Schimmel, M., Mangeney, A. & Patau, G., 2012. Modelling long-term seismic noise in various environments, *Geophys. J. Int.,* **191**(2), 707–722.

Tanimoto, T., 2005. The oceanic excitation hypothesis for the continuous oscillations of the earth, *Geophys. J. Int.,* **160**(1), 276–288.

Tarantola, A. & Nercessian, A., 1984. Three-dimensional inversion without blocks, *Geophys. J. Int.,* **76**(2), 299–306.

Tarantola, A. & Valette, B., 1982. Generalized nonlinear inverse problems solved using the least squares criterion, *Rev. Geophys.,* **20**(2), 219–232.

Traer, J. & Gerstoft, P., 2014. A unified theory of microseisms and hum, *J. geophys. Res.,* **119**(4), 3317–3339.

Wapenaar, K., 2004. Retrieving the elastodynamic Green's function of an arbitrary inhomogeneous medium by cross correlation, *Phys. Rev. Lett.,* **93**(25), doi:10.1103/PhysRevLett.93.254301.

Weaver, R.L. & Lobkis, O.I., 2006. Diffuse fields in ultrasonics and seismology, *Geophysics,* **71**(4), SI5–SI9.

Webb, S.C., 2007. The Earth's hum is driven by ocean waves over the continental shelves, *Nature,* **445**(7129), 754–756.

APPENDIX A: SYNTHETIC TESTS AND TOMOGRAPHIC MODEL COMPARISON

To estimate the resolution of our tomographic model, we performed several synthetic tests. We also compared our model with three published models and quantified the differences.

A1 Synthetic tests

In this section, we present the synthetic tests. As the inversion is separated into two steps, we checked the lateral and vertical resolutions separately. The lateral resolution is estimated with synthetic tests of group-velocity regionalisation. The vertical resolution is tested with synthetic tests of group-velocity inversion *versus* depth, to retrieve the *S*-wave velocity.

We used checkerboard tests to investigate the model lateral resolution. We constructed synthetic group-velocity maps for the real path coverage. The inversion was performed with the same correlation length (800 km) and *a-priori errors*, as for the real data. The resolution is considered good when the checkerboard image is reconstructed. Figs A1(a) and (b) show that anomalies of 2000 km width are well recovered for latitudes between 72°N and 54°S. At higher latitudes, the resolution decreases due to the absence of seismic stations. Figs A1(c) and (d) show that anomalies of 3000 km width are well recovered between 81°N and 54°S.

We then tested the local group-velocity inversion *versus* depth to retrieve the *S*-wave velocity model. Figs A1(e)–(h) show four synthetic tests with two delta-like anomalies separated by 100 km. We compare the case of two positive (e) and two negative (f) anomalies and one positive and one negative anomaly (g) and (h). We observe that the two anomalies are recovered and well separated in all four cases. The inversion can resolve two anomalies separated by 100 km in the depth range of 50–300 km with a smoothing effect that increases with depth. This vertical smoothing effect is due partly to the smoothing parameters of the inversion, and mostly to the different sensitivities of the surface waves with depth.

A2 Tomographic model comparison

We compared our HUM2 model with three published *S*-wave velocity models. We selected the SV velocity model of Nishida *et al.* (2009), which is the only other tomographic model derived solely from hum data. It is here called NMK2009. They computed cross-correlations between 54 stations and stacked 17 yr of correlograms.

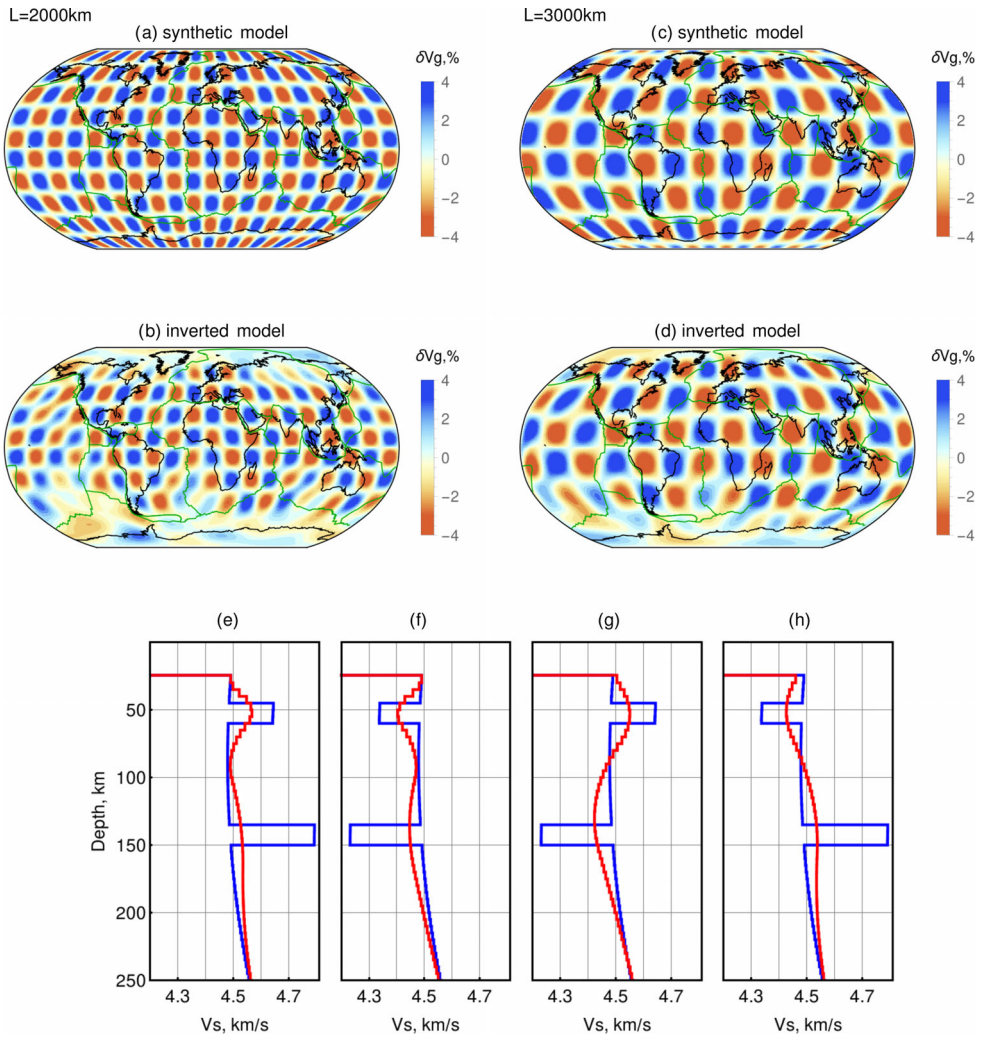

Figure A1. Synthetic tests to estimate the horizontal (a)–(d) and vertical (e)–(h) resolution. Synthetic group-velocity model with positive and negative anomalies of 2000 km (a) and 3000 km (c) width. Inverted group-velocity map (b) and (d) corresponding to maps (a) and (b), respectively. Anomalies of 2000 km width are well recovered except at high latitude. (e)–(h) show synthetic (blue) and inverted (red) *S*-wave velocity models. The two delta-like anomalies are separated by 90 km, and they are well recovered.

Their model is derived from 906 R1 trains and 777 R2 trains of Rayleigh wave phase velocity measurements in the period band of 120–375 s. The two other models are obtained from earthquake data. One model is the global upper-mantle SV velocity model of Debayle & Ricard (2012), here called DR2012, which is derived from 375 000 Rayleigh waveform seismograms. They used fundamental and higher Rayleigh mode phase velocity measurements. The other model is from Auer *et al.* (2014), here called SAVANI, which is a radially anisotropic *S* velocity model based on published data sets of surface wave phase velocities and body-wave traveltimes.

We computed the Pearson's correlation between the four models as a function of depth as follows:

$$r = \frac{\sum_i (x_i - \bar{x})(y_i - \bar{y})}{\sqrt{\sum_i (x_i - \bar{x})^2}\sqrt{\sum_i (y_i - \bar{y})^2}} \quad \text{(A1)}$$

where x_i and y_i are velocity model perturbations at location (latitude, longitude) i for model A and B, respectively, and $\bar{x}$ and $\bar{y}$ are the means of x_i and y_i. Fig. A2 shows the correlation between all four of these models. The correlation between our HUM2 model and DR2012 and SAVANI is high, at about 0.90 between 80 and

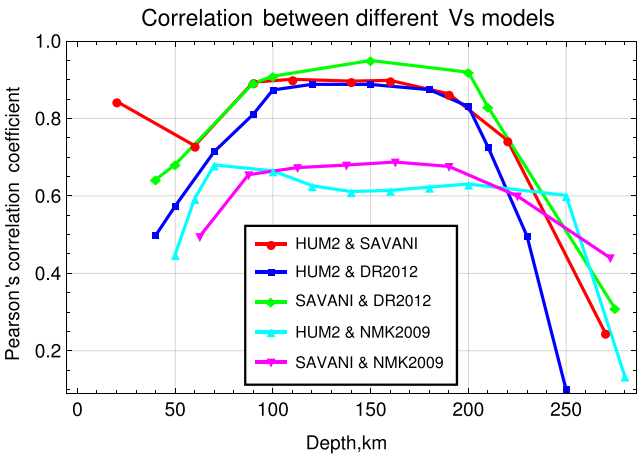

Figure A2. Pearson correlations between our model (HUM2), and the three published models: NMK2009 from Nishida *et al.* (2009), DR2012 from Debayle & Ricard (2012) and SAVANI from Auer *et al.* (2014), as a function of depth.

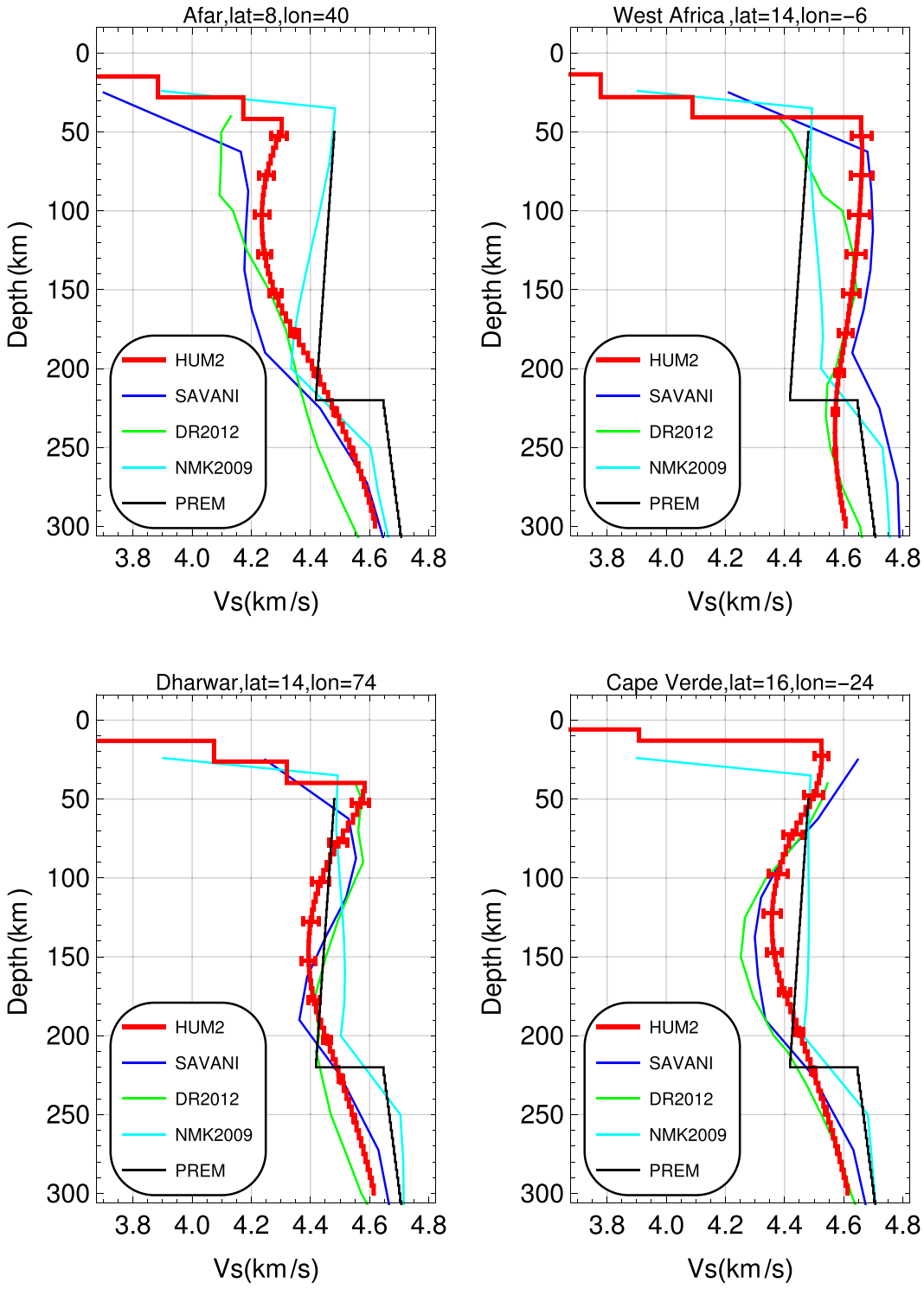

Figure A3. *S*-wave velocity as a function of depth at four locations: Afar, the West Africa craton, the Dharwad craton and Cape Verde. Five models are plotted for comparison: our model (HUM2) as reference with uncertainties, and the three published models: NMK2009 from Nishida *et al.* (2009) in light blue, DR2012 from Debayle & Ricard (2012) in green and SAVANI from Auer *et al.* (2014) in dark blue. The PREM *Vs* model is plotted in black.

200 km in depth. Correlation between HUM2 and NMK2009 is much lower, at 0.6, but similar to the correlation between SAVANI and NMK2009, which is 0.7. This might be due to the lower resolution of NMK2009, which is derived from a smaller data set than the other models.

Below 80 km and above 220 km, correlations between all of the models decrease. At shallow depths, this might be due to crustal correction that might be differently implemented. At large depth (deeper than 200 km), models HUM2, SAVANI and DR2012 have different sensitivities due to the different seismic phases measured

(fundamental mode, higher modes and/or body waves), which can explain the decrease in the correlation. Our model is only derived from the fundamental mode Rayleigh waves, and it progressively loses resolution below 200 km in depth.

Fig. A3 shows a comparison of *S*-wave velocity models as a function of depth for two cratons and two hotspots.

APPENDIX B: *S*-WAVE VELOCITY TRANS-DIMENSIONAL INVERSION

This appendix describes the group-velocity inversion to retrieve the local *S*-wave velocity model.

For a given *S*-wave velocity model, synthetic group velocities, $U_{\rm syn}(T)$, as a function of periods, T, are computed following Saito (1988). The sphericity of the Earth and the frequency dependence of the *S*-wave velocity model are taken into account using the Earth flattening transformation (Biswas & Knopoff 1970) and eq. (3) of Dziewonski & Anderson (1981), respectively.

The *S*-wave velocity model to be retrieved is represented as a weighted sum of B-spline basis functions defined as follows:

$$V_S(z) = V_S^0(z) + \sum_{m=0}^{M-1} V_m N_{m,2}(z), \tag{B1}$$

where $N_{m,2}(z)$ is the mth non-uniform quadratic B-spline basis function (De Boor 1978), M is the number of B-spline basis functions, V_m are weight coefficients, $V_S^0(z)$ is the *a priori* reference Earth model that is composed of the crust2.0 model (Laske *et al.* 2013) and the PREM with smoothed 220 km discontinuity. Whenever the crust2.0 is thinner than the PREM crust, the PREM uppermost mantle structure is extrapolated up to the bottom of the new crust.

The trans-dimensional inversion is a composition of two nested loops: for a given spline basis $\{N_{m,2}\}$, the inner loop computes the optimum model weight coefficients (V_m) and the outer loop determines the optimum spline basis.

The inner loop uses the simulated annealing optimization algorithm (Press 2007, chap. 10.9) to minimize the misfit function:

$$\chi_d^2 = \frac{1}{N}\sum_{n=1}^{N}\left[U_{\rm obs}(T_n) - U_{\rm syn}(T_n)\right]^2/\sigma_d^2(T_n), \tag{B2}$$

where $U_{\rm obs}$ and $U_{\rm syn}$ are the measured and synthetic group velocities, T_n is the period, σ_d is the measurement error and N is the number of periods.

The outer loop uses the golden section search in one dimension (Press 2007, chapter 10.1) to minimize the expression $(\chi_d^2 + \chi_m^2)/2$ as a function of the number of splines M, where χ_d^2 is the result of inner-loop minimization of eq. (B2) and χ_m^2 is the model variance quantity defined as:

$$\chi_m^2 = \frac{1}{M}\sum_{m=0}^{M-1}\sigma_m^2/\Delta^2, \tag{B3}$$

where Δ is the *a-priori* model variance that acts as a regularisation parameter. We compute σ_m^2 as the diagonal elements of the model covariance matrix $\mathbf{C}_m$, as estimated by (Menke 2012):

$$\mathbf{C}_m = \mathbf{G}^{-g}\mathbf{C}_d\mathbf{G}^{-gT}, \tag{B4}$$

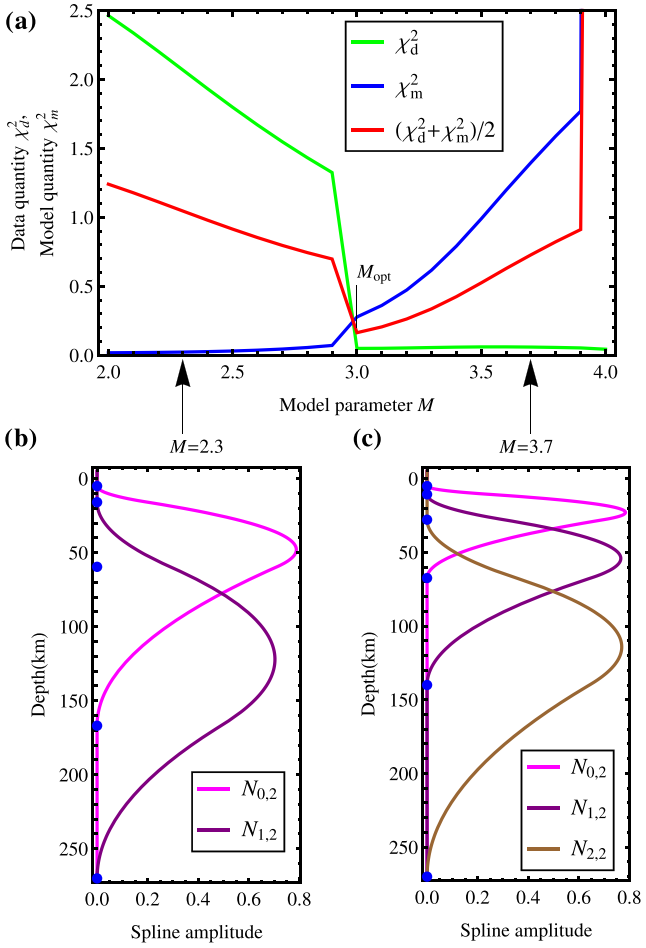

Figure B1. (a) Misfit χ_d^2 and model variance χ_m^2 as functions of spline basis. The integer values of parameter M correspond to the number of splines in the bases and $M_{\rm opt}$ is the selected spline basis. (b) and (c) Spline bases for $M = 2.3$ and $M = 3.7$, respectively.

where $\mathbf{C}_d$ is the data covariance matrix with diagonal elements $\sigma_d^2(T_n)$, $\mathbf{G}$ is the partial derivative matrix of the group velocity $U_{\rm syn}(T_n)$ with respect to the spline weight V_m, that is, $G_{mn} = \partial U_{\rm syn}(T_n)/\partial V_m$ and '-g' indicates the generalized inverse.

The number of splines M in the outer loop minimization can be considered as continuous. This depends on the number of knots P as follows: $M = P - 3$. P is calculated as the depth range of the model divided by the variable interval between the knots. We start from equidistant knots, the normalized depths of which are called x, and convert these through the transformation $y(x) = bx + (1 - b)x^a$. The new knot depths are now condensed to the top of the model. Figs B1(b) and (c) show two examples of B-spline bases for $M = 2.3$ and $M = 3.7$, respectively, and their corresponding knots (blue points). The functions χ_d^2 and χ_m^2 as a function of the number of splines M are shown in Fig. B1(a), by the green and blue lines, respectively. This illustrates a trade-off between fitting the dispersion curves and model uncertainty. The best compromise between these is for the optimal number of splines $M = M_{\rm opt}$. It was found by trial and error that optimal values for the parameters a and b can be assigned arbitrarily in the intervals of $3 < a < 4$, $0.2 < b < 0.4$.